A Radon-based criterion for the energy resolution of photon counting x-ray detectors

Nicolas Ducros, T Johng-Ay, M Arques, P Douek, F Peyrin

A Radon-based criterion for the energy resolution of photon counting x-ray detectors

N. Ducros[1], **T. Johng-Ay**[1], **M. Arques**[2], **P. Douek**[1], **F. Peyrin**[1]

[1] Univ Lyon, INSA-Lyon, Université Lyon 1, CNRS, Inserm, CREATIS UMR 5220 U1206, 7 Av. Jean Capelle, F-69621, Villeurbanne, France
[2] CEA Léti, Département micro Technologies pour la Biologie et la Santé, Laboratoire détecteurs, Minatec Campus, 17 rue des martyrs, F-38054 Grenoble Cedex

E-mail: nicolas.ducros@creatis.insa-lyon.fr

14 March 2016

Abstract. Thanks to recent developments in photon counting detectors, X-Ray spectral imaging has received increasing attention. This technique permits the quantification of the chemical components in an object. The energy selectivity of the detector is known to have a strong impact in the material decomposition capabilities of an imaging device. Although spectral imaging devices are widely used in conjunction to polychromatic illuminations, detectors are typically characterized for one or few incident energies. To the best of our knowledge, no criterion for the overall energy resolution of a photon counting detector is available yet. In this paper, we propose a criterion for energy selectivity over a range of incident energies. Our criterion is based on the analysis of the response of the detector to multiple monochromatic illuminations. In particular, it can be easily computed from the Radon transform of the energy response function of the detector. After a simulation study, we show how this criterion is related to the quality of material decompositions obtained from photon counting measurements.

Keywords: Spectral X-ray imaging, photon counting detectors, energy resolution, performance criterion, Radon transform.

Submitted to: *Phys. Med. Biol.*

1. Introduction

X-ray spectral imaging is raising increasing interest in radiology owing to the new clinically relevant contrasts it can deliver. Similarly to dual-energy X-ray imaging, material decomposition algorithms can be used to recover the individual contribution of a pair of constituent materials, e.g. soft tissue and bone (Alvarez and Macovski, 1976). The most promising capability of spectral imaging is often considered to be K-edge imaging that can quantitatively resolve heavy elements such as iodine, gold, bismuth, or gadolinium (Feuerlein et al., 2008; Schlomka et al., 2008; Shikhaliev, 2012;

Cassol Brunner et al., 2013). When targeted contrast agents carry a payload with a K-edge element, spectral X-ray spectral imaging allows for molecular imaging. It has been shown that the concentration of the constituents of the human body such as bone, water, fat or concentration in contrast agents, can be recovered (Schirra et al., 2014). Prototypes of such systems are already available for small animal imaging but not yet for clinical imaging since there are still some issues related to detectors, exploitation of data, and inversion schemes (Anderson and Butler, 2014).

X-ray spectral imaging has emerged thanks to the development of a new generation of photon counting detectors (PCD) with energy discrimination capabilities (Taguchi and Iwanczyk, 2013). Spectral detectors can classify X-ray photons into different energy bins depending on their energy. Current PCDs offer a limited number of output energy bins, e.g. from 2 to 8, which are defined according to some energy thresholds (Taguchi and Iwanczyk, 2013). Although the imaging capabilities of X-ray spectral devices are closely related to the energy discrimination capabilities of the detector (Roessl et al., 2011; Potop et al., 2014), it is still not clear how energy discrimination should be characterized. The energy resolution of a PCD is sometimes understood as the width and/or numbers of the energy bins (Feuerlein et al., 2008; Lee et al., 2012). The optimal number of bins and their bounds are object-dependent and their determination is still the subject of active research (Cassol et al., 2015, 2016). Moreover, although detectors are expected to count the photons within given energy bins, some photons may be misclassified due to different physical phenomena such as fluorescence, share sharing, or photon pile-up (Taguchi and Iwanczyk, 2013). This behavior is illustrated by the response of the detector to monochromatic illuminations. So far, the energy resolution of a PCD has been widely characterized considering the full-width-at-half-maximum (FWHM) of the detector response function (Fredenberg et al., 2010; Taguchi et al., 2011; Wang et al., 2011; Saha, 2012; Macias-Montero et al., 2015). Equivalently, the standard deviation obtained by fitting a Gaussian model (Jakubek, 2011; Myronakis and Darambara, 2011; Myronakis et al., 2012) or an error function (Xu, Persson, Chen, Karlsson, Danielsson, Svensson and Bornefalk, 2013; Xu, Chen, Persson, Karlsson, Danielsson, Svensson and Bornefalk, 2013) was considered. However, the resulting energy resolution depends on the energy of the monochromatic illumination, typically as the square root of the latter (Fredenberg et al., 2010). Since photon-counting detectors aim at measuring simultaneously photons at different energies, the aforementioned criteria do not directly translate into image quality.

The goal of the paper is to provide a single criterion that is able to account for the energy resolution of a PCD over a range of incident energies. We propose a new criterion, which is based on the analysis of the energy response function (ERF) of the detector, and demonstrate that it can be easily computed from the Radon transform of the ERF. Further, it is shown that the criterion is closely related to the quality of the material decompositions obtained from the ERFs corresponding to the same detector operating at different fluxes.

In section 2, we recall the basis of spectral X-ray imaging and material decomposition. In section 3, we introduce the quality criterion and describe our simulations in a thorax phantom. In section 4, the computation of the quality criterion for different ERFs is discussed together with the resulting material decompositions.

2. Theory

2.1. Measured signal

Let us consider an object defined inside the spatial domain Ω and characterized at energy E by its attenuation coefficient $\mu(\boldsymbol{r}, E), \boldsymbol{r} \in \Omega$. The object is imaged by a detector that lies in the plane Σ. The number of photons transmitted through the object and reaching the detector at position $\boldsymbol{u} \in \Sigma$ is given by the line integral

$$n(\boldsymbol{u}, E) = n_0(E) \exp\left(-\int_{\mathcal{L}} \mu(\boldsymbol{r}, E)\, \mathrm{d}\boldsymbol{r}\right) \tag{1}$$

where $n_0(E)$ is X-ray the source spectrum, $\mathcal{L}$ is the path of integration that depends on the acquisition geometry. The signal s_i output in the energy bin $[\mathcal{E}_i, \mathcal{E}_{i+1}], i = 1 \dots I$, at the pixel location $\boldsymbol{u}$ may be modeled by

$$s_i(\boldsymbol{u}) = \iint_{[\mathcal{E}_i, \mathcal{E}_{i+1}] \times \Re} d(\mathcal{E}, E)\, n(E, \boldsymbol{u})\, \mathrm{d}E\, \mathrm{d}\mathcal{E} \tag{2}$$

where $d(\mathcal{E}, E)$ is a probability density function that accounts for the probability of a photon reaching the detector at energy E to be detected at energy $\mathcal{E}$. In the following it is referred to as energy response function (ERF).

The bounds of the energy bins $[\mathcal{E}_i, \mathcal{E}_{i+1}]$ depend on the values chosen for some counter thresholds in the ASIC (Taguchi and Iwanczyk, 2013). In practice, only electronic thresholds (e.g. voltage, current, LSB, or charge) can be set. Therefore, associating the electronic thresholds threshold to energy bounds requires to calibrate the device.

2.2. Material decomposition through polynomial calibration

The signals $s_i(\boldsymbol{u}), i = 1 \dots I$, can be exploited to recover chemical composition of the object. The standard approach consists in decomposing the object onto a basis of two materials (Alvarez and Macovski, 1976). In this case, the attenuation of the object is assumed to satisfy

$$\mu(\boldsymbol{r}, E) = \rho_1(\boldsymbol{r})\tau_1(E) + \rho_2(\boldsymbol{r})\tau_2(E) \tag{3}$$

where τ_m, $m \in \{1, 2\}$ is the mass attenuation coefficient (in $\mathrm{cm}^2.\mathrm{g}^{-1}$) of the mth material and ρ_m its density in $\mathrm{g.cm}^{-3}$. Inserting Eq. (3) into Eq. (1) :

$$n(\boldsymbol{u}, E) = n_0(E) \exp\left[-a_1(\boldsymbol{u})\tau_1(E) - a_2(\boldsymbol{u})\tau_2(E)\right] \tag{4}$$

where

$$a_m(\boldsymbol{u}) = \int_{\mathcal{L}} \rho_m(\boldsymbol{r})\, \mathrm{d}\boldsymbol{r}, \quad \forall m \in \{1, 2\} \tag{5}$$

is the mass of material m projected along $\mathcal{L}$. It has units of $\mathrm{g.cm}^{-2}$.

The material decomposition problem consists in finding the mass vector $\boldsymbol{a} = [a_1, \dots a_M]^\top$ from the measurement vector $\boldsymbol{s} = [s_1, \dots s_I]^\top$ for all the pixels of the detector. The solution proposed by Alvarez and Macovski (1976) consists in assuming the following polynomial relationship

$$\boldsymbol{a} = \mathcal{P}(\boldsymbol{s}) \tag{6}$$

where $\mathcal{P}$ is a second order polynomial. Then, the material decomposition problem is solved by a two-step algorithm.

- *Step 1: calibration of* $\mathcal{P}$. Measurements from known calibration phantoms are acquired. The polynomial coefficients are then tuned to minimize the difference between the calibration lengths and the lengths modeled by Eq. (6). Let $\mathcal{P}^*$ denote the retained polynomial.
- *Step 2: decomposition.* The solution is readily given by

$$\boldsymbol{a}^* = \mathcal{P}^*(\boldsymbol{s}) \tag{7}$$

3. Method

3.1. Definition of the quality criterion

The ERF d in Eq. (2) is a detector response function that characterizes the detector. It can be obtained experimentally repeating measurements for various incoming monochromatic X-ray beams, which can be achieved at synchrotron sources (Schlomka et al., 2008). It can also be obtained numerically considering Monte-Carlo simulations that take into account the physics of the detectors scintillator (Myronakis and Darambara, 2011; Lee et al., 2012). For a typical ERF (see Fig. 5), a photon incoming at a given energy can be classified in any of the different output energy bin. This energy dispersion intrinsically defines the quality of a spectral detector. Three physical phenomena are essentially involved in the detection process. Each translates to one of the three lines that can be observed in the ERFs of Fig. 5. The lower diagonal line, referred to as *main ridge* in the following, represents the probability to detect photons in the correct energy bin, the upper diagonal line indicates the detection of fluorescence photons, and the horizontal line results from charge sharing between adjacent pixels (refer to Taguchi and Iwanczyk 2013 for details).

From the previous observation, we introduce the discrimination ability $Q(\alpha)$ of a detector as the probability of a photon to be classified in the correct energy bin with a precision α (keV). Mathematically,

$$Q(\alpha) = \frac{N(\alpha)}{N_{\text{tot}}} \tag{8}$$

where $N(\alpha)$ is the number of photons that are detected in the window of width α keV that is centered about the ridge of the detector response and N_{tot} is the total number of detected photons. By definition, the discrimination ability is a normalized quantity ranging from 0 to 1.

3.2. Computation of the quality criterion

We propose to compute $Q(\alpha)$ by means of the Radon transform of the detector response. The Radon transform associates to an image its integrals over the different lines of the plane. While the Radon transform is extensively used in tomography, it is also used in image analysis to identify lines in images. Since a line in the image domain is mapped to a point in the Radon domain, the Radon transform has been a traditional tool for the identification of lines in images (Deans, 2007). Here, the Radon transform is used for both identifying the ridge of the detector response and computing the quality criterion itself. We propose the following two-step approach

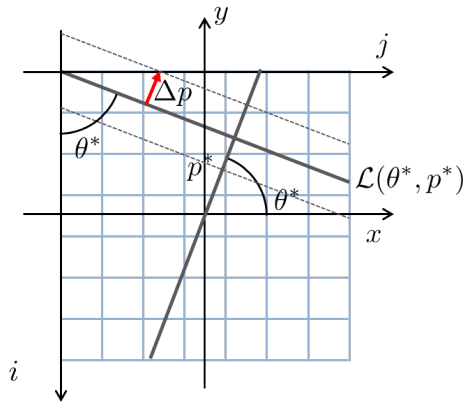

Figure 1. Figure of principle and notations for the computation of the $\mathcal{Q}_\alpha$ criterion

3.2.1. Extraction of the main ridge We assume that the largest coefficient in the Radon transform of the detector response maps to the main ridge of the detector response. Then, the ridge is mathematically given by the pair of parameters

$$(\theta^*, p^*) = \underset{(\theta,p)\in[0,\pi)\times\mathbb{R}}{\arg\max} \mathcal{R}\{d\}(\theta, p) \tag{9}$$

where $\mathcal{R}\{\cdot\}$ is the Radon transform of a two-dimensional function along the line $\mathcal{L}(\theta, p) = \{(x, y) \,|\, p = x\cos\theta + y\sin\theta\}$ (Kak and Slaney, 1988, chap. 3). The notations are depicted on Fig. 1.

3.2.2. Computation of the quality criterion in the Radon domain The quality criterion can now be easily computed in the Radon domain. Indeed, we have

$$N(\alpha) = \int_{p^*-\Delta p(\alpha)}^{p^*+\Delta p(\alpha)} \mathcal{R}d(\theta^*, p)\mathrm{d}p \tag{10}$$

and

$$N_{\mathrm{tot}} = \int_{\mathbb{R}} \mathcal{R}d(\theta^*, p)\mathrm{d}p. \tag{11}$$

where $\Delta p(\alpha)$ is the width of the integration window in pixels.

3.2.3. Discretisation and implementation Let the input and output energy bins j and i related to the input and output energies by $E = j\Delta E$ and $\mathcal{E} = i\Delta\mathcal{E}$. Computing the discrete Radon transform of the matrix $(d_{i,j})$ with $d_{i,j} = d(i\Delta\mathcal{E}, j\Delta E)$ in a coordinate system having its origin at the center of the detector response, the equation of the ridge is given by

$$i = \frac{j - j_0}{\tan\theta^*} - \frac{p^*}{\sin\theta^*} + i_0 \tag{12}$$

where (i_0, j_0) are the coordinates of the center of the detector response.

In practice, $\Delta\mathcal{E}$ is unknown and can hardly be determined *a priori*. An interesting feature of the proposed approach is that the width of the output energy bin can be

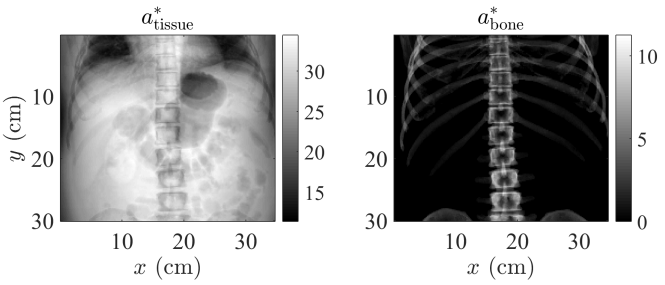

Figure 2. Numerical phantom. Mass attenuation of the projected mass of soft tissue (left) and bone (right) in units of g.cm^2

recovered using the relationship

$$\Delta\mathcal{E} = \tan\theta^* \Delta E \tag{13}$$

The demonstration is provided in Appendix A. Inserting Eq. (13) into Eq. (12), we obtain the following relationship between output and input energies with units of keV

$$\mathcal{E} = E - E_0 - \frac{p^* \Delta E}{\cos\theta^*} + \mathcal{E}_0 \tag{14}$$

where $(\mathcal{E}_0, E_0)$ are the coordinates of the centre of the detector response matrix expressed in keV.

Since the Radon transform is performed on a discretised version of the detector response function, it is important to note that Δp is expressed in pixel. However, it is related to α with units of keV by

$$\Delta p = \frac{\alpha}{\Delta E} \cos\theta^* \tag{15}$$

The demonstration is provided in Appendix B.

3.3. Numerical experiments

3.3.1. Phantom We considered the 3D thorax phantom that was segmented from a CT scan (Kechichian et al., 2013). The attenuation of the object has been computed considering $M = 2$ material, namely soft tissues and bones. Each voxel has been associated to the mass attenuation of whether soft tissues or bone, according to the segment it belongs to. Mass attenuations were taken from ICRU report 44 (ICRU, 1989). Then, the material density in each voxel was estimated from the CT images. As given in Eq. (5), projected masses for each material are finally computed integrating densities along lines chosen perpendicular to the coronal plane. The resulting projected masses are illustrated on Fig. 2.

3.3.2. Synthetic data The source spectrum $n_0(E)$ was simulated by the *SpekCalc* program (Poludniowski, 2007; Poludniowski et al., 2009) setting the anode angle to 12° and inherent filtration to 1.2 mm Al. Different tube potentials were considered,

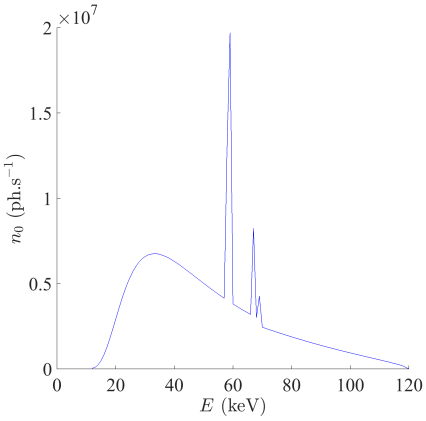

Figure 3. Source spectra used for all the simulations.

resulting in a peak energy $E_{\max}$ ranging from 70 keV to 120keV. The resulting spectra are depicted on Fig. 3. Different detector responses were simulated at increasing X-ray photon flux, considering photons with energy ranging from 10 to 140 keV (Gorecki et al., 2013). Measurements were corrupted by Poisson noise assuming 10^7 X-ray photons reached each pixel of the detector, which corresponds for a pixel of 1.7mm^2 to a dose before patient of 396 μGy. We considered dual-energy measurements, i.e. $I = 2$ energy-dependent images were computed. Low-energy measurements are obtained summing up photons in the energy bin $[\mathcal{E}_1, \mathcal{E}_2]$ and high-energy measurements in the energy bin $[\mathcal{E}_2, \mathcal{E}_3]$, with $\mathcal{E}_1 = 10$ keV and $\mathcal{E}_3 = E_{\max}$. Determining the best value for $\mathcal{E}_2$ is a multi-parameter problem that typically depends on the images to be decomposed, i.e. the phantom itself. Here, material decompositions have been performed for $\mathcal{E}_2$ in the range $[10, E_{\max}]$ keV and the CNR of the decomposed bone image is used to determined the best $\mathcal{E}_2$ that we denote $\mathcal{E}_2^*$. The material decomposition was performed by means of polynomial calibration, as described in section 2.2, imposing the recovery of $M = 2$ materials, namely soft tissues and bone.

3.4. Figure of merit

To evaluate the quality of the decomposed images, the contrast-to-noise (CNR) ratio was considered. This performance metric is based on the definition of two regions in the image, namely the region of interest (ROI) Σ_{roi} and background region (BR) Σ_{back}. The CNR is defined by

$$\text{CNR} = \frac{|\mu_{\text{roi}} - \mu_{\text{back}}|}{(\sigma_{\text{roi}}^2 + \sigma_{\text{back}}^2)^{\frac{1}{2}}} \tag{16}$$

where μ_{roi} (resp. μ_{back}) indicated the mean value of the recovered masses in the ROI (resp. BR) and σ_{roi} (resp. σ_{back}) the standard deviation of the recovered masses in the ROI (resp. BR).

In practice, the ROI includes all the bone pixels and the BR consists of the surrounding pixels. The BR is easily obtained by subtracting the ROI to dilated version of ROI. The size of the structuring element for the dilation is chosen in order

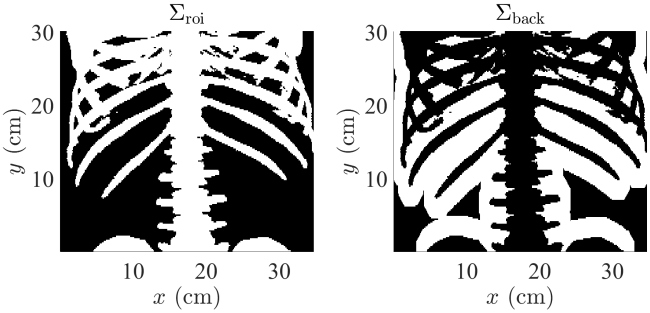

Figure 4. (a) Region of interest (ROI) and (b) background region (BR) used for the computation of the CNR as defined by Eq. (16). The regions are indicated in white.

to get a number of pixels in the BR that is as close as possible to the number of pixels in the ROI. Both ROI and BR are depicted on Fig. 4.

4. Results and discussion

4.1. Computation of Q_α

The detector response function of the same detector has been simulated at increasing flux ranging from 0.5 to 150 μGy.s^{-1}. The detector response at the 4 lowest fluxes is displayed on Fig. 5. It can be observed that the higher the flux, the more photons are spread over high energies. This is a well known issue in spectral X-ray imaging known as photon pile-up. If two photons hit the detector in a short period of time, the detector may be unable to treat the two events independently, which results in the detection of whether one photon with an overestimated energy or two photons with erroneous energies.

The discrimination ability $\mathcal{Q}$ has been computed for all the 6 ERFs. The main ridge recovered by our method is superimposed on the ERFs displayed one Fig. 5 together with the energy window for a precision α of 10 keV. There are two main difficulties in extracting the main ridge. First, the horizontal line due to charge sharing may correspond to large coefficients in the Radon domain. The main ridge being expected to be at angles lower than 90°, the computation of the Radon transform was restricted to $\theta \in [5, 85]°$. Second, the Radon transform may show local maxima close in value to the global one, in particular for ERFs simulated at high flux. This is a numerical problem that is mainly due to the sampling of the discrete Radon transform. It can be alleviated by smoothing the Radon transform along p with a moving average filter. The length of the filter is chosen to be $\frac{\beta}{\Delta E}\cos\theta$, which is equivalent to recovering a ridge of width β. In this work we chose $\beta = 1$ keV. The matlab code we developed is provided as supplementary material. It can be observed on Fig. 5 that the main ridge was successfully recovered in all cases with our method.

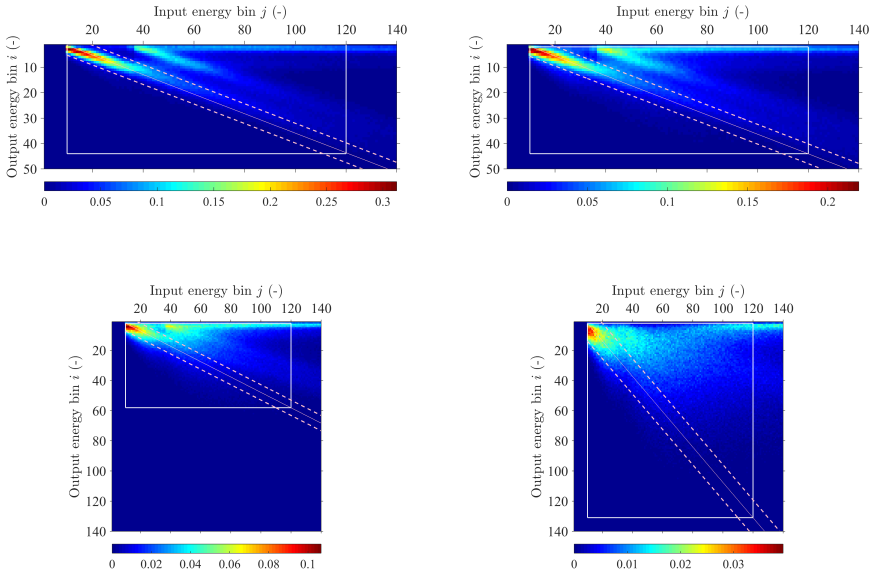

Figure 5. Energy response function (ERF) of the same detector operating at increasing flux (from top left to bottom right). Incoming photons with energy ranging from 10 to 140 keV are considered. The main ridge recovered by our method is indicated by the full line, the integration window for $\alpha = 10$ keV by the dotted line.

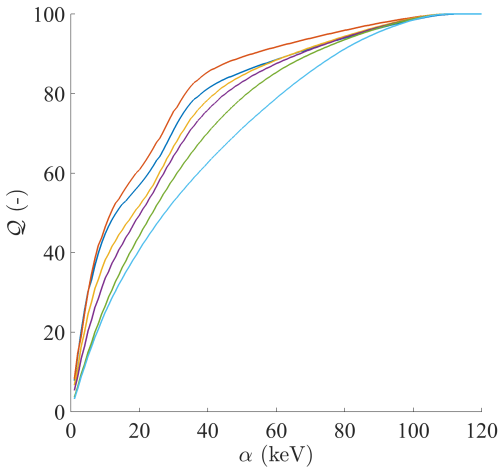

Figure 6. Evolution of the Q criterion as function of the precision α for different detector responses simulated at increasing flux (from top to bottom).

The output bin width $\Delta\mathcal{E}$ is provided in Table 1. The higher the flux, the larger $\Delta\mathcal{E}$, which is consistent with the energy spreading effect of photon pile-up.

Fig. 6 plots the discrimination ability $\mathcal{Q}$ as a function of the integration window

flux	μGy.s^{-1}	0.5	1.5	5	15	50	150
$\Delta\mathcal{E}$	keV	3.27	3.38	2.61	2.61	1.96	0.85
$Q(10\,\text{keV})$	%	41.0	40.2	37.8	33.1	26.3	25.0
$\alpha_{0.5}$	keV	13.2	11.7	18.4	20.4	23.8	27.4
i_2^*	-	15	16	16	18	22	50
$\mathcal{E}_2^*$	keV	50.3	50.0	52.4	54.4	51.0	51.7
CNR	-	1.21	1.21	1.20	1.16	1.02	0.57

Table 1. Some metrics for a detector response simulated at different fluxes

α. As expected, $\mathcal{Q}$ is monotonically increasing with α in the range $[0, 1]$. It is observed that the higher the flux, the lower the discrimination ability whatever the integration window. Hence, the $\mathcal{Q}$ criterion is found to be a good metric metrics for the energy spreading due to the photon pile-up that can be visually observed on Fig. 5.

Finally, we compute the integration window that corresponds to a discrimination ability of 50%. It is reported in Table 1 where it is denoted $\alpha_{0.5}$. It increases from about 13 keV to 27 keV increasing the flux by a factor 300. We suggest $\alpha_{0.5}$ as an indicator of the spectral resolution of a detector.

4.2. Relation between the discrimination ability and the material decomposition quality

In order to verify that $Q(\alpha)$ can be used as a metric of the performance of a spectral detector, we performed material decomposition from the same simulated data set considering the six previous detector responses. The estimated decompositions of bone and soft tissue are illustrated on Fig. 7 showing qualitatively the degradation of the results with the flux. The corresponding CNR are provided in Table 1. As expected, it is observed that the higher the flux, the lower the CNR of the material decomposition. The decomposed images obtained from data measured at 0.5, 1.5 and 5 μGy.s^{-1} were very similar (compare the CNRs for instance) and were not all displayed. Note that the reported CNRs have been obtained from the dual-energy data set corresponding to the best energy binning. The optimum energy threshold is provided in Table 1 in both bin numbers (see i_2^*) and keV units (see $\mathcal{E}_2^*$). Interestingly, it can be noted that the threshold expressed in keV is almost constant whatever the ERF, which shows the interest of the energy calibration feature of our method.

5. Conclusion

We introduced a criterion that accounts for the energy selectivity of X-ray spectral detectors. It was shown that this criterion correlates well with the material decomposition capabilities of a detector. Our approach to compute the discrimination ability is two-step. The first step consists in calibrating the energy response function of the detector, which proved useful for fixing the thresholds of our multi-energy acquisitions.

Here, the computation of the discrimination ability was used to assess the impact of photon pile-up for a given detector architecture. However, we believe that this criterion could be also be of interest in the comparison of detector architectures, e.g. sandwich vs monolayer.

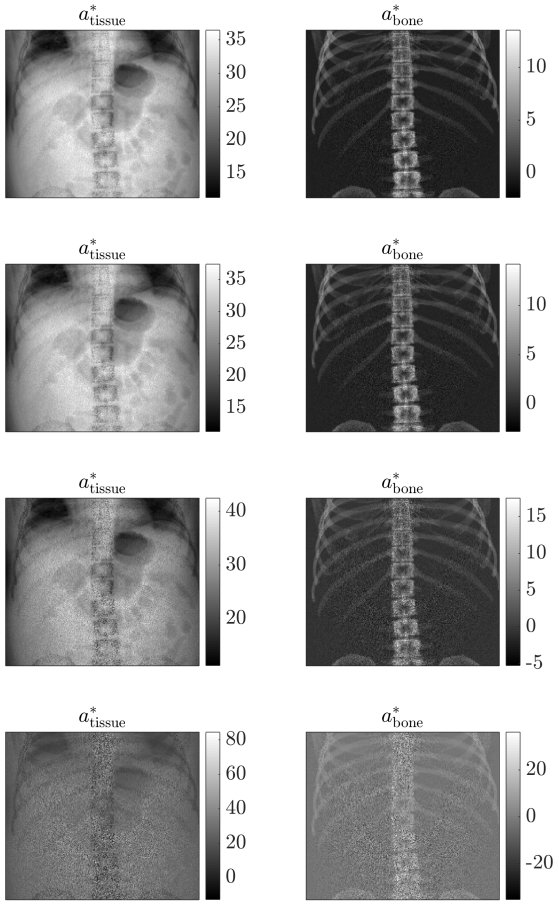

Figure 7. Material decomposition results for detector response simulated at increasing flux (from top to bottom). The recovered mass of soft tissue is displayed on the left, the recovered mass of bone on the right

6. Acknowledgment

This work was funded by the Agence Nationale pour la Recherche under Grant ANR-12-TECS-0002-03. It was performed within the framework of the LABEX PRIMES (ANR-11-LABX-0063) of Université de Lyon, within the program "Investissements d'Avenir" (ANR-11-IDEX-0007) operated by the French National Research Agency (ANR).

The authors are grateful to R. Kéchichian and S. Valette for providing them with the 3D thorax phantom. They would also like to thank S. Rit and J.M. Létang for fruitful discussions about materiel decomposition.

Appendix A. Width of the output energy bin

The main ridge $\mathcal{L}(\theta^*, p^*)$ is used to 'calibrate' the output energy step $\Delta\mathcal{E}$, i.e. $\Delta\mathcal{E}$ is chosen such that an increase of the input energy is mapped to the same increase of

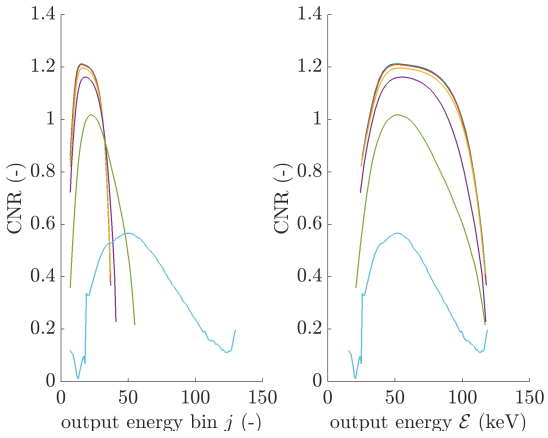

Figure 8. CNR for DRM at various fluxes. CNR is plotted against the energy bin index (left) and the output energy obtained thanks to Eq. (13) (right).

the output energy. Mathematically, we chose

$$\Delta i \Delta \mathcal{E} = \Delta j \Delta E, \quad \forall (i,j) \in \mathcal{L}(\theta^*, p^*) \tag{A.1}$$

where Δj (resp. Δi) denotes an increase of the number of input (resp. output) energy bins. Any pair of indices (i,j) belonging to the main ridge satisfying Eq. (12), we have

$$\Delta j = \Delta i \tan\theta^*, \tag{A.2}$$

Inserting Eq. (A.2) into Eq. (A.1) leads to

$$\Delta \mathcal{E} = \Delta E \tan\theta^*. \tag{A.3}$$

Appendix B. Length of the integration window

We start projecting the integration window Δp onto the input energy bin axis (refer to Fig. 1). We have

$$\Delta p = \Delta j \cos\theta^* \tag{B.1}$$

where Δj is the corresponding number of input bins. Note that Δj has no unit. The corresponding width in keV is $\Delta j \Delta E$. By definition of α, we impose

$$\alpha = \Delta j \Delta E \tag{B.2}$$

Plugging the previous equation into Eq. (B.1), we finally obtain

$$\Delta p = \frac{\alpha}{\Delta E} \cos\theta^* \tag{B.3}$$

References

Alvarez R E and Macovski A 1976 *Physics in Medicine and Biology* **21**(5), 733.
URL: *http://stacks.iop.org/0031-9155/21/i=5/a=002*

Anderson N G and Butler A P 2014 *Contrast Media & Molecular Imaging* **9**(1), 3–12.
URL: *http://dx.doi.org/10.1002/cmmi.1550*

Cassol Brunner F, Dupont M, Meessen C, Boursier Y, Ouamara H, Bonissent A, Kronland-Martinet C, Clemens J, Debarbieux F and Morel C 2013 *Nuclear Science, IEEE Transactions on* **60**(1), 103–108.

Cassol F, Dupont M, Kronland-Martinet C, Ouamara H, Dawiec A, Boursier Y, Bonissent A, Clémens J C, Portal L, Debarbieux F and Morel C 2016 *Biomedical Physics & Engineering Express* **2**(2), 025003.
URL: *http://stacks.iop.org/2057-1976/2/i=2/a=025003*

Cassol F, Portal L, Graber-Bolis J, Perez-Ponce H, Dupont M, Kronland C, Boursier Y, Blanc N, Bompard F, Boudet N, Buton C, Clémens J C, Dawiec A, Debarbieux F, Delpierre P, Hustache S, Vigeolas E and Morel C 2015 *Physics in Medicine and Biology* **60**(14), 5497.
URL: *http://stacks.iop.org/0031-9155/60/i=14/a=5497*

Deans S R 2007 *The radon transform and some of its applications* Dover Publications Mineola, N.Y. "This Dover edition, first published in 2007, is an unabridged republication of the 1993 edition, published by Krieger Publishing Company, Malabar, Florida, containing corrections and updated references, of the work originally published by John Wiley and Sons, Inc., New York, in 1983.".
URL: *http://catdir.loc.gov/catdir/enhancements/fy0743/2007016162-d.html*

Feuerlein S, Roessl E, Proksa R, Martens G, Klass O, Jeltsch M, Rasche V, Brambs H J, Hoffmann M H K and Schlomka J P 2008 *Radiology* **249**(3), 1010–1016.
URL: *http://radiology.rsna.org/content/249/3/1010.abstract*

Fredenberg E, Lundqvist M, Cederström B, Åslund M and Danielsson M 2010 *Nuclear Instruments and Methods in Physics Research Section A: Accelerators, Spectrometers, Detectors and Associated Equipment* **613**(1), 156 – 162.
URL: *http://www.sciencedirect.com/science/article/pii/S0168900209021044*

Gorecki A, Brambilla A, Moulin V, Gaborieau E, Radisson P and Verger L 2013 *Journal of Instrumentation* **8**(11), P11011.
URL: *http://stacks.iop.org/1748-0221/8/i=11/a=P11011*

ICRU 1989 Report 44 of the tissue substitutes in radiation dosimetry and measurement Technical report International Commission on Radiation Units and Measurements (ICRU).

Jakubek J 2011 *Nuclear Instruments and Methods in Physics Research Section A: Accelerators, Spectrometers, Detectors and Associated Equipment* **633, Supplement 1**, S262 – S266. 11th International Workshop on Radiation Imaging Detectors (IWORID).
URL: *http://www.sciencedirect.com/science/article/pii/S0168900210013732*

Kak A C and Slaney M 1988 *Principles of Computerized Tomographic Imaging* IEEE Press New York.

Kechichian R, Valette S, Desvignes M and Prost R 2013 *Image Processing, IEEE Transactions on* **22**(11), 4224–4236.

Lee S W, Choi Y N, Cho H M, Lee Y J, Ryu H J and Kim H J 2012 *Physics in medicine and biology* **57**(15), 4931–4949.

Macias-Montero J G, Sarraj M, Chmeissani M, Martinez R and Puigdengoles C 2015 *IEEE Transactions on Nuclear Science* **62**(5), 2327–2333.

Myronakis M E and Darambara D G 2011 *Medical Physics* **38**(1), 455–467.
URL: *http://scitation.aip.org/content/aapm/journal/medphys/38/1/10.1118/1.3532825*

Myronakis M E, Zvelebil M and Darambara D G 2012 *Journal of Instrumentation* **7**(03), P03004.
URL: *http://stacks.iop.org/1748-0221/7/i=03/a=P03004*

Poludniowski G G 2007 *Medical Physics* **34**(6), 2175–2186.
URL: *http://scitation.aip.org/content/aapm/journal/medphys/34/6/10.1118/1.2734726*

Poludniowski G, Landry G, DeBlois F, Evans P M and Verhaegen F 2009 *Physics in Medicine and Biology* **54**(19), N433.
URL: *http://stacks.iop.org/0031-9155/54/i=19/a=N01*

Potop A, Rebuffel V, Rinkel J, Brambilla A, Peyrin F and Verger L 2014 Vol. 9033 pp. 90333I–90333I–10.
URL: *http://dx.doi.org/10.1117/12.2042133*

Roessl E, Brendel B, Engel K, Schlomka J P, Thran A and Proksa R 2011 *IEEE Transactions on Medical Imaging* **30**(9), 1678–1690.

Saha G B 2012 *Physics and radiobiology of nuclear medicine* Springer Science & Business Media.

Schirra C O, Brendel B, Anastasio M A and Roessl E 2014 *Contrast media & molecular imaging* **9**(1), 62–70.

Schlomka J P, Roessl E, Dorscheid R, Dill S, Martens G, Istel T, Baumer C, Herrmann C, Steadman R, Zeitler G, Livne A and Proksa R 2008 *Physics in Medicine and Biology* **53**(15), 4031.
URL: *http://stacks.iop.org/0031-9155/53/i=15/a=002*

Shikhaliev P M 2012 *Physics in Medicine and Biology* **57**(6), 1595.
URL: *http://stacks.iop.org/0031-9155/57/i=6/a=1595*

Taguchi K and Iwanczyk J S 2013 *Medical Physics* **40**(10), 100901.
URL: *http://link.aip.org/link/?MPH/40/100901/1*

Taguchi K, Zhang M, Frey E C, Wang X, Iwanczyk J S, Nygard E, Hartsough N E, Tsui B M W and Barber W C 2011 *Medical Physics* **38**(2), 1089–1102.
URL: *http://link.aip.org/link/?MPH/38/1089/1*

Wang X, Meier D, Mikkelsen S, Maehlum G E, Wagenaar D J, Tsui B M W, Patt B E and Frey E C 2011 *Physics in Medicine and Biology* **56**(9), 2791.
URL: *http://stacks.iop.org/0031-9155/56/i=9/a=011*

Xu C, Chen H, Persson M, Karlsson S, Danielsson M, Svensson C and Bornefalk H 2013 *Nuclear Instruments and Methods in Physics Research Section A: Accelerators, Spectrometers, Detectors and Associated Equipment* **715**, 11 – 17.
URL: *http://www.sciencedirect.com/science/article/pii/S0168900213002180*

Xu C, Persson M, Chen H, Karlsson S, Danielsson M, Svensson C and Bornefalk H 2013 *Nuclear Science, IEEE Transactions on* **60**(1), 437–445.